Crack initiation mechanisms under two stress ratios up to very-high-cycle fatigue regime for a selective laser melted Ti-6Al-4V

Leiming Du [a,b], Xiangnan Pan [a], Guian Qian [a], Liang Zheng [b,*], Youshi Hong [a,*]

[a] LNM, Institute of Mechanics, Chinese Academy of Sciences, Beijing 100190, China
[b] School of Science, Harbin Institute of Technology, Shenzhen 518055, China

ARTICLE INFO

ABSTRACT

Crack initiation mechanisms under two stress ratios ($R = -1$ and 0.5) and up to very-high-cycle fatigue (VHCF) regime of a selective laser melted (SLMed) Ti-6Al-4V were investigated. Type I lack-of-fusion defects (almost equiaxed) induced crack initiation except for the cases of VHCF under $R = 0.5$ in which type II defects (large aspect ratio) caused facet mode crack initiation. A nanograin layer formed underneath the crack initiation region of rough area for the cases of VHCF at $R = -1$, which was explained by the numerous cyclic pressing (NCP) model. A P-S-N approach was introduced to well describe the fatigue life up to VHCF regime under $R = -1$ and 0.5 for the SLMed titanium alloy.

1. Introduction

Additive manufacturing (AM) is an advanced manufacturing technology that is capable of fabricating complex and near-net shape components directly from a 3D computer designed model by material feedstock in a layer by layer process [1–4]. Selective laser melting (SLM) is one of the most applicable AM techniques, in which the powder of desired material is selectively melted via a high power laser beam thus having the capability of melting the material powder completely to get almost full density parts. However, one critical concern of SLM is that the defects inevitably exist [5,6], which are detrimental to mechanical properties, especially the fatigue performance of the selective laser melted (SLMed) parts. Therefore, it is necessary to investigate the fatigue behavior of SLMed parts to ensure a safety application.

The titanium components fabricated by SLM have gained a lot of attentions due to their high specific static and fatigue strength. As reported in Refs. [7,8], the quasi-static mechanical properties of SLMed parts were comparable or even better than those of wrought ones due to the fine microstructure resulted from the high thermal gradients in the SLM process. However, the fatigue resistance of titanium parts made by AM is much lower than conventionally built ones [9,10]. This is primarily caused by the presence of defects in the AM parts, and the defects act as fatigue crack initiation origins due to the stress concentration generated in the surrounding material [11]. As a result, AM parts exhibit lower fatigue resistance than their forged counterparts, and their fatigue data display significant uncertainty with large scatter, which are mainly ascribed to the defect propensities of size, shape, location and spacing [12–14].

A number of studies on forged titanium alloys have shown that fatigue failure can occur beyond 10^7 loading cycles, i.e. very-high-cycle fatigue (VHCF) [15–17]. The decrease in fatigue strength in VHCF regime is associated with the change in failure mode from surface cracking induced fracture in low-cycle fatigue (LCF) and high-cycle fatigue (HCF) regime to internal cracking induced fracture in VHCF regime [18,19]. Many previous studies have focused on LCF [20,21] and HCF [22,23] properties of AM titanium alloys. Recently, several results with respect to the VHCF behavior of AM titanium alloys are available in the literature [24–26]. Günther et al. [24] found that crack initiation location shifted from specimen surface to interior when the fatigue life changed from HCF to VHCF regime for an SLMed Ti–6Al–4V. Qian et al. [25] established a probabilistic S-N (P-S-N) model based on the defect size distribution to describe the VHCF strength at 10^9 cycles for an SLMed Ti-6Al-4V, which decreased with the building orientation from 0° to 90°, while the crack initiation sites of the broken specimens were always from internal defects at both HCF and VHCF regimes. In addition, our recent study [26] showed that the fatigue strength of SLMed titanium specimens in HCF and VHCF regimes remarkably decreases with the increase of porosity percentage. For conventional titanium alloys, internal cracks originated from the cleavage of α phase [27]. For SLMed Ti-6Al-4V alloys, however, fatigue cracks usually initiated from internal

---

* Corresponding authors.
E-mail addresses: icon_lzheng@hit.edu.cn (L. Zheng), hongys@imech.ac.cn (Y. Hong).
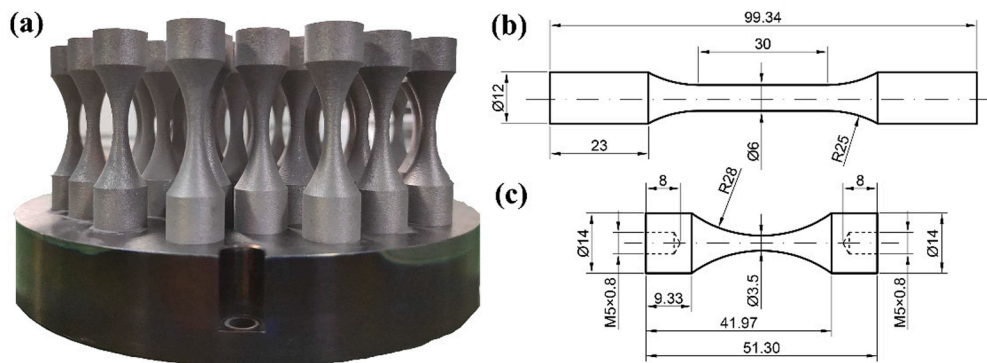
Fig. 1. Manufactured specimens used for fatigue tests (a), shape and dimensions (mm) of specimens for tensile tests (b), and for ultrasonic fatigue tests (c).

lack-of-fusion defects [26], for which, the detailed characteristics of crack initiation in relation to the defects under different stress ratios are little understood and need further investigations.

Moreover, it is reported that the value of mean stress or stress ratio (*R*) has a significant effect on the HCF and VHCF properties of forged titanium alloys with bimodal [27], equiaxed [28] or lamellar-equiaxed [29] microstructures. As an example, Liu et al. [27] revealed that faceted crack initiation dominates the failure mode in HCF and VHCF regimes of a forged Ti–6Al–4V alloy, and the number of facet crack initiation sites increased with the increase of stress ratio. The microstructure evolution underneath the crack initiation region (rough area, RA) also differs under negative or positive stress ratios in VHCF regime [29]. Nanograin layer formed underneath the fracture surface within the RA region of a forged Ti–6Al–4 V at $R = -1$, while no nanograins were presented in the crack initiation region at $R = 0$ and 0.5. With regard to this, Hong et al. [30] proposed the "numerous cyclic pressing (NCP)" model to explain the formation mechanism of nanograins in VHCF for high-strength steels, which has been confirmed being valid for the RA of forged titanium alloys [28,29,31]. However, the role of stress ratio in the damage process of HCF and VHCF for SLMed titanium alloys is rarely reported and the related crack initiation mechanism is unclear. Thus the crack initiation mechanism under different stress ratios in HCF and VHCF regimes for SLMed titanium alloys deserves in-depth investigations.

In this paper, the crack initiation mechanisms up to VHCF regime under negative and positive stress ratios for an SLMed Ti-6Al–4V were investigated. First, ultrasonic fatigue tests (20 kHz) were performed on the specimens under the stress ratios of −1 and 0.5. Then, the fracture surfaces were examined by scanning electron microscopy (SEM) and the crack initiation modes at different stress ratios were classified. Moreover, the analyses via focused ion beam (FIB) microscopy and transmission electron microscopy (TEM) were conducted to characterize the microstructure of the crack initiation region. Finally, a fatigue strength prediction model based on the obtained S-N data and defect size distribution was introduced. The P-S-N curves and fatigue strengths up to VHCF regime at different stress ratios were well described by the model.

2. Test material and experimental methods

The tensile and fatigue specimens were fabricated by a commercial HBD-200 additive manufacturing system. Pre-alloyed gas-atomized Ti-6Al-4V powder with the particle size between 19 and 50 μm was used. The main chemical composition of the powder consists of 6.40 wt% Al, 4.10 wt% V and balance Ti. All specimens were fabricated vertically on a base plate with the processing parameters optimized in our previous research [26] with laser power of 160 W, layer thickness of 30 μm, scan speed of 1200 mm/s and hatch spacing of 0.07 mm. The combination of such processing parameters gives the input laser energy density *E* of 76.2 J/mm³ [26], which was calculated by the following formula [32].

$$E = \frac{P}{v \cdot h \cdot t} \tag{1}$$

where *P* is laser power (J s⁻¹), *v* is scan speed (mm s⁻¹), *h* is hatch spacing (mm) and *t* is layer thickness (mm).

Fig. 1a shows the SLMed Ti-6Al-4V specimens used for fatigue tests. A post-SLM heat treatment at 600 °C for 2 h followed by cooling under argon atmosphere was performed to relieve the residual stresses produced in the SLM process. Additionally, all specimens were polished to a mirror finish prior to the tests to minimize the effects of surface imperfections arising from partially-melted powder particles.

For the microstructure examination of the SLMed Ti-6Al-4V, two samples were cut from a fatigue specimen in the annealed state by spark cutting, and the samples were ground by using sandpapers. The cross sections of the samples were polished with a suspension of 50 nm nano-
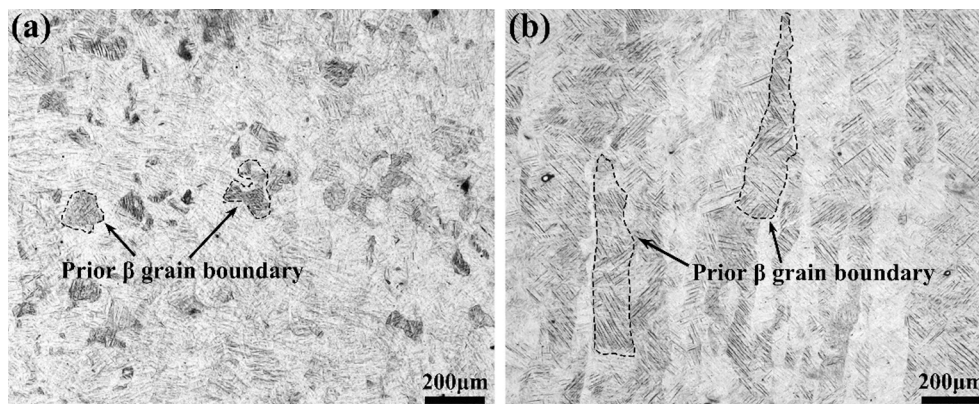

Fig. 2. OM images showing microstructure of SLMed samples (a) horizontal cross-section, and (b) longitudinal cross-section.
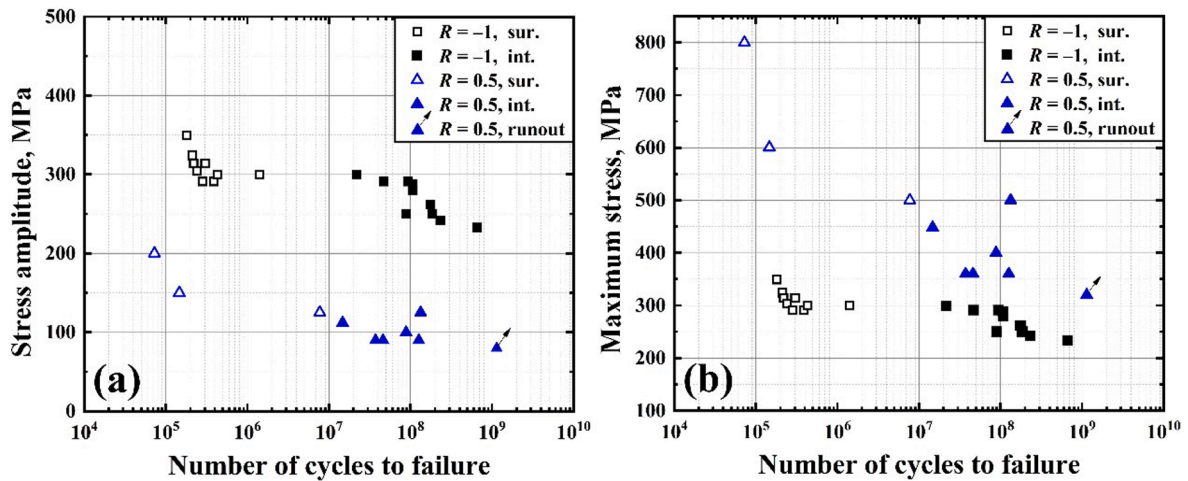
Fig. 3. S-N data of test material for $R = -1$ and 0.5. (a) In terms of stress amplitude versus fatigue life, and (b) in terms of maximum stress versus fatigue life. sur.: surface crack initiation, int.: internal crack initiation.

SiO_2 and H_2O_2, and then etched by Kroll reagent for about 10 s. Finally, the microstructures of both vertical and horizontal cross-sections were examined by using an Olympus GX71 optical microscope (OM). Due to the rapid cooling and high temperature gradient for the specimens in the SLM process, the microstructure of the SLMed Ti-6Al-4V is almost acicular α′ martensites within columnar prior β grains, similar to the case in Ref. [33]. It is worth noting that the SLMed Ti-6Al-4V specimens annealed at 600 °C that is below the β phase transformation temperature will not result in any notable change in microstructure morphology [34]. Fig. 2a shows the microstructure of the horizontal cross-section,

which consists of almost acicular α′ martensites transformed from prior β grains. Fig. 2b shows the microstructure of the longitudinal cross-section. It is clearly observed that large columnar grains of prior β phases are almost oriented along the build direction, epitaxially growing across multiple deposition layers up to hundreds of microns. This microstructure is frequently observed in additively manufactured parts, resulting in strong anisotropic mechanical properties [35].

Monotonic tensile tests were conducted on four specimens via a servo-hydraulic system at a strain rate of 10^{-4} s^{-1}. The shape and the dimensions of the specimen with a gage length of 30 mm and a diameter
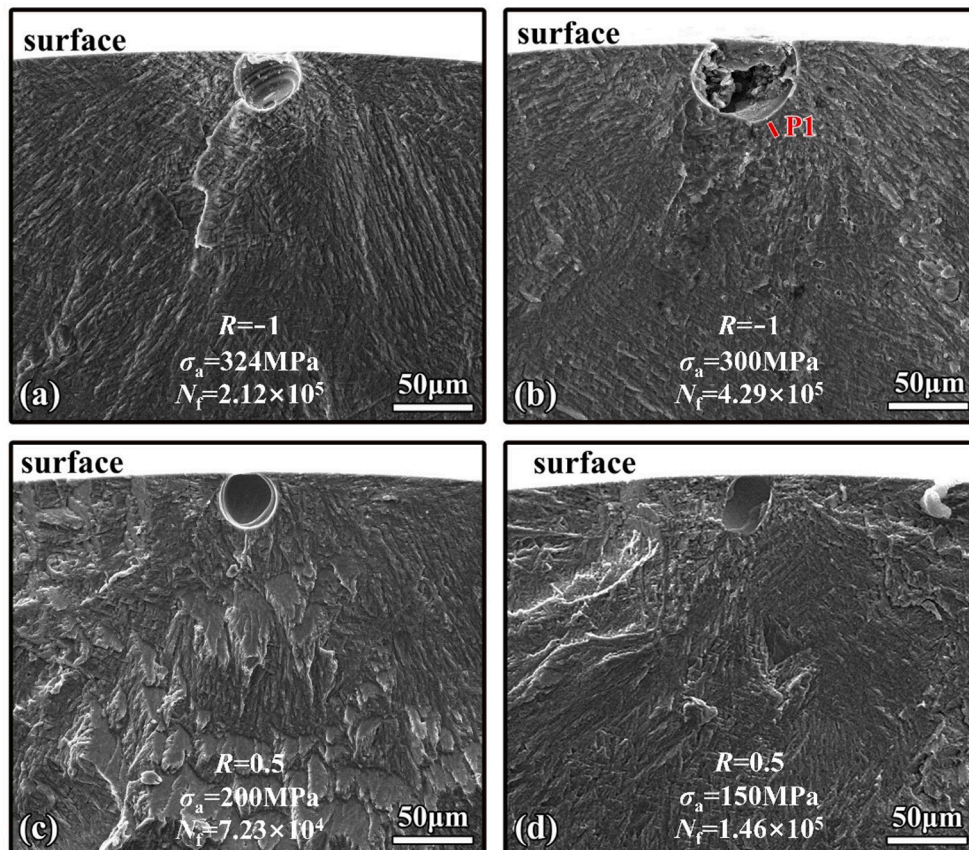

Fig. 4. Typical fracture surface morphologies of crack initiation from surface defects of specimens failed in LCF and HCF regimes, P1 in (b) being the location of TEM sample cut by FIB.
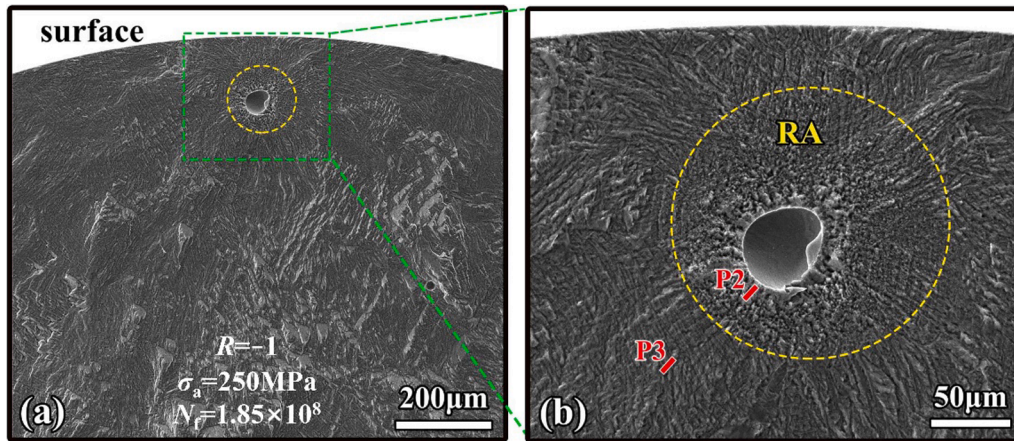
Fig. 5. Typical fracture surface morphologies of crack initiation from internal defects of specimens failed in VHCF regime at $R = -1$, P2 and P3 in (b) being the location of TEM sample cut by FIB.

of 6 mm are shown in Fig. 1b. The loading axis was parallel to the build direction. The results are: yield strength (σ_y) 1045 ± 5 MPa, ultimate tensile strength (σ_u) 1200 ± 10 MPa and total elongation (ε_t) 4 ± 0.2%. The tensile strength agrees well with the results ranging from 1006 to 1327 MPa reported in the literature [36]. The strain to failure is relatively low but also within the range between 1.6 and 11.9% reported in the literature [36]. Studies (e.g. Ref. [37]) have shown that the quasi-static mechanical performance of SLMed Ti-6Al-4V alloy is controlled by the related microstructure and defects. Since the SLMed Ti6Al4V is majorly composed of fine and acicular α′ martensites, it is reasonable that the strength of such a titanium alloy is higher than that of the counterpart produced by conventional methods. Although the metallurgical defects have little impact on the monotonic tensile strength, they have detrimental effects on the total elongation as reported in Ref. [26].

The fatigue tests were conducted on an ultrasonic vibration machine (Lasur GF20-TC) at 20 kHz, which was installed in a conventional tensile machine (capacity 20 kN) to enable the ultrasonic cycling under an amount of mean stress. The ultrasonic specimens were specially designed into an hourglass shape with a minimum diameter of 3.5 mm to ensure the resonant frequency of the specimen equal to the input incitation frequency (20 ± 0.5 kHz) of the piezoelectric ceramic resonator. The shape and dimensions of the specimen for ultrasonic fatigue tests are shown in Fig. 1c. During the ultrasonic fatigue testing, the compressive air was used to cool the specimen to ensure that the possible temperature rise of the test specimen was negligible. After the fatigue tests, fracture surfaces of all failed specimens were examined by a field-emission type of scanning electron microscope (SEM, FEI QUANTA 200 FEG), and the failure types and crack initiation sites were identified. Moreover, the size and distribution of the defects on the fracture surfaces were measured by using Image-Pro Plus 6.0 software. Then the Gumbel distribution [38] of the defects was obtained and used in the P-S-N modeling.

By means of focused ion beam (FIB) technique with a dual beam (FIB-SEM) system FEI Helios Nanolab 600i, five FIB samples from the selected crack initiation sites were prepared for detail observation of the microstructure underneath the crack initiation and early growth region
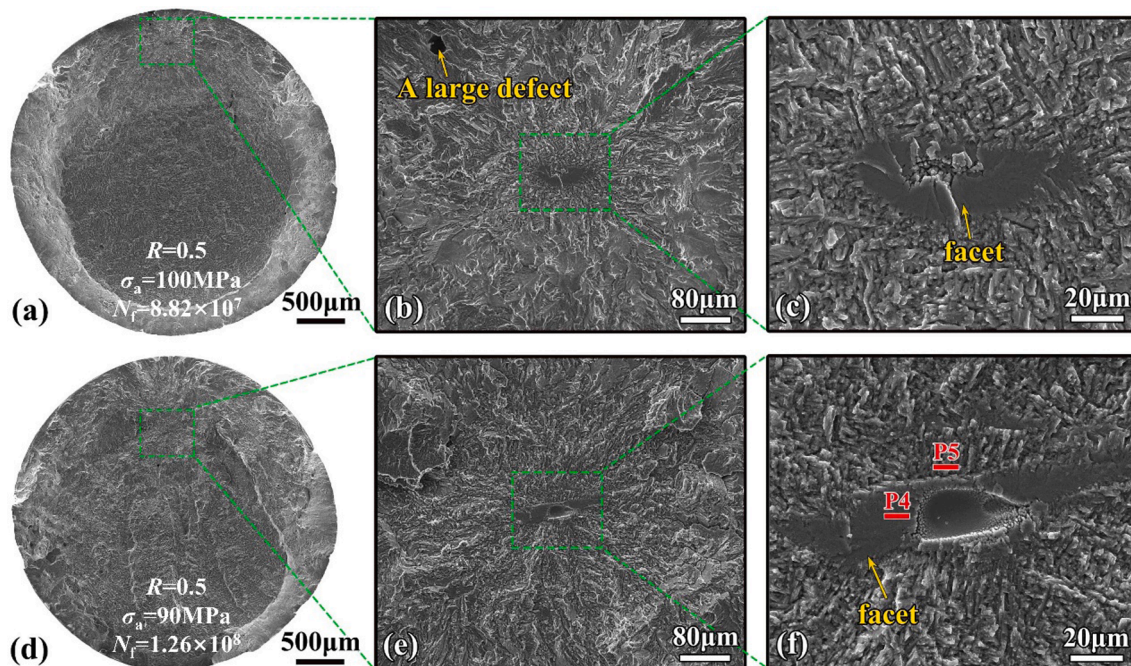

Fig. 6. Typical fracture surface morphologies of crack initiation from internal defects of specimens failed in VHCF regime at $R = 0.5$, P4 and P5 in (f) being the location of TEM sample cut by FIB.

for fatigue failed specimens, and then were examined by transmission electron microscopy (TEM) with selected area electron diffraction (SAD) via an FEI Tecnai G2 F30 S-Twin. The diameter of the electron diffraction area was 200 nm, and a platinum (Pt) layer was coated to protect the fracture surface of the extracted samples during FIB cutting process.

3. Results and discussion of crack initiation mechanisms

3.1. S-N data and fractographic morphologies

Fig. 3a shows the obtained S-N data in terms of applied stress amplitude σ_a versus fatigue life N_f with the stress ratios of −1 and 0.5, which cover the fatigue life from 10^4 to 10^9 cycles. For the stress ratio of −1, the S-N curve presents a step-wise trend. The fatigue strength σ_a of specimens from 10^5 to 10^7 cycles varied from 350 MPa to 290 MPa and decreased to 225 MPa at 10^9 cycles. While for the stress ratio of 0.5, the S-N curve exhibits a continuously descending trend. The fatigue strength σ_a from 10^4 to 10^7 cycles varied from 200 MPa to 115 MPa and decreased to 100 MPa at 10^9 cycles. Fig. 3b shows the data of maximum stress σ_{max} versus N_f under the two stress ratios of −1 and 0.5. The maximum stress σ_{max} at $R = 0.5$ varied from 320 MPa to 800 MPa. It is seen from this figure that at a certain fatigue life, the maximum stress level for $R = 0.5$ is much larger than that for $R = -1$.

SEM observations showed that surface crack initiation is dominant in HCF regime and internal crack initiation prevails in VHCF regime for the SLMed Ti-6Al-4V specimens failed at both cases of $R = -1$ and 0.5, which is also indicated in Fig. 3 by hollow and solid symbols, respectively. When the fatigue life N_f was less than 10^7 cycles, fatigue cracks initiated from surface defects as shown in Fig. 4. The surface defects that induced crack initiation are of regular shape (almost equiaxed) at both negative stress ratio ($R = -1$) and positive stress ratio ($R = 0.5$). This indicates that stress ratio has little effect on the crack initiation pattern for the case of surface crack initiation. However, when the fatigue life N_f was larger than 10^7 cycles, fatigue cracks initiated from internal defects as shown in Fig. 5 ($R = -1$) and Fig. 6 ($R = 0.5$). It is seen that the fracture surface morphologies of the specimens that failed from internal defects under stress ratio of $R = -1$ are different from those of $R = 0.5$, which will be further addressed in the following Sections 3.2 and 3.3.

Fig. 5 shows the fracture surface of the specimen failed at 1.85×10^8 cycles under $R = -1$. The entire region of crack initiation and early propagation marked with dashed curve exhibits a rough area (RA) with fine granular feature on the fracture surface, which is similar to the fine granular area (FGA) for high-strength steels in VHCF regime. RA or FGA is the characteristic region of crack initiation in VHCF for titanium alloys or high-strength steels, whose formation period consumed a majority part of total fatigue life [16,30,31]. Different from the SLMed Ti-6Al-4V, almost no defects (cavities or inclusions) were found at the crack initiation sites for conventionally produced titanium alloys with bimodal [27] or equiaxed [28] microstructure. Their fatigue cracks originated from the cleavage of α phase and then the coalescence of facets formed an RA on the fracture surface.

For the case of $R = 0.5$, there was no rough area feature on the fracture surface of the specimens experienced VHCF as shown in Fig. 6. Instead, a rather smooth cleavage-like region surrounding the crack origin appears as shown in Fig. 6c and f. Thus, it is inferred that the RA region formed only in the crack initiation region of the SLMed Ti-6Al-4V during VHCF at $R = -1$. The microstructural details in the crack initiation region will be characterized in the following Section 3.3.

3.2. Two types of defects to induce crack initiation

From Figs. 4–6, two types of defects were observed at crack initiation sites. It is defined that type I defect is the lack-of-fusion defects with regular shape (almost equiaxed), which induced crack initiation in HCF and VHCF regimes for the stress ratio of $R = -1$ as shown in Fig. 4a, b and Fig. 5, and in HCF regime for the stress ratio of $R = 0.5$ as shown in
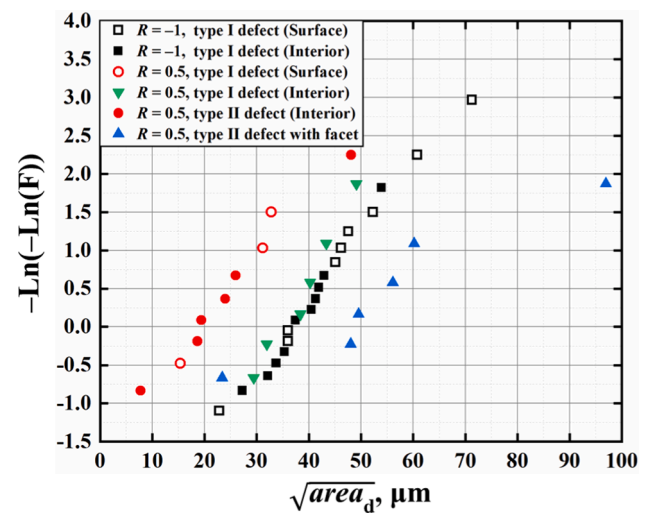

Fig. 7. Gumbel plot of defect sizes at $R = -1$ and 0.5; type I defect referring to lack-of-fusion defects with regular shape (almost equiaxed), and type II defect referring to lack-of-fusion defects with irregular shape (large aspect ratio).

Fig. 4c and d. Type II defect is defined as the lack-of-fusion defects with irregular shape (large aspect ratio), which induced crack initiation in VHCF regime for the stress ratio of $R = 0.5$ as shown in Fig. 6. Interestingly, a lamellar facet appears, which embraces the type II defect that acts as the crack origin as shown in Fig. 6c and f. It is very likely that the facet was generated due to the localized stress concentration at the defect-matrix boundary.

For the further characterization of the crack initiation propensity caused by different types of defects, the sizes of the defects observed on the fracture surfaces of failed specimens were measured by the use of Image-Pro Plus 6.0 software. Fig. 7 shows the Gumbel plot of the measured defect sizes. The horizontal axis $\sqrt{area_d}$ is the equivalent defect size, and the vertical axis $-(Ln(-Ln(F)))$ is the reduced variate, which follows the cumulative function distribution of the Gumbel extreme value analysis. It is seen that the sizes of original type II defects in the specimens subjected to VHCF under $R = 0.5$ are smaller than those of original type I defects, and the sizes of type II defects with facets are significantly larger than those of type I defects. In addition, the sizes of type I defects that were observed on the fracture surface but did not result in crack initiation at $R = 0.5$ are close to the sizes of type I defects observed in the crack initiation region at $R = -1$. Because the distribution of defect sizes in every specimen of the present batch is statistically the same, thus it is suggested that the state of stress ratio (mean stress) may alter the crack initiation mechanism. A fatigue crack may originate from a relatively smaller type II defect to form a facet domain surrounding the defect as shown in Fig. 6b, although the prevalence of relatively larger type I defects in the specimen. It is inferred that the high level of mean stress causes the occurrence of a crystallographic facet from the type II defect and the new formed facet defect becomes more fatal in the fatigue damage than the existed type I defects.

The change of crack initiation mechanism from type I to type II defects has following reasons. On the one hand, the shape of defect influences the process of crack initiation. Because the specimens were fabricated in the vertical direction, the axis of the defects are normal to the loading direction [39] and the irregular defect possesses sharp edges, which tend to increase local stress concentration at the tip of a sharp edge. On the other hand, the crack closure effect also influences the process of crack initiation. For the case of $R = 0.5$, the maximum stress σ_{max} is larger than that of $R = -1$ and the crack tip is always under the state of opening stress, which promotes the facet formation. While for the case of $R = -1$, the compressive part of the far field stress induces the compressive stress at the localized field of initiated crack surfaces to cause crack closure [29], which may retard facet formation, i.e., type I
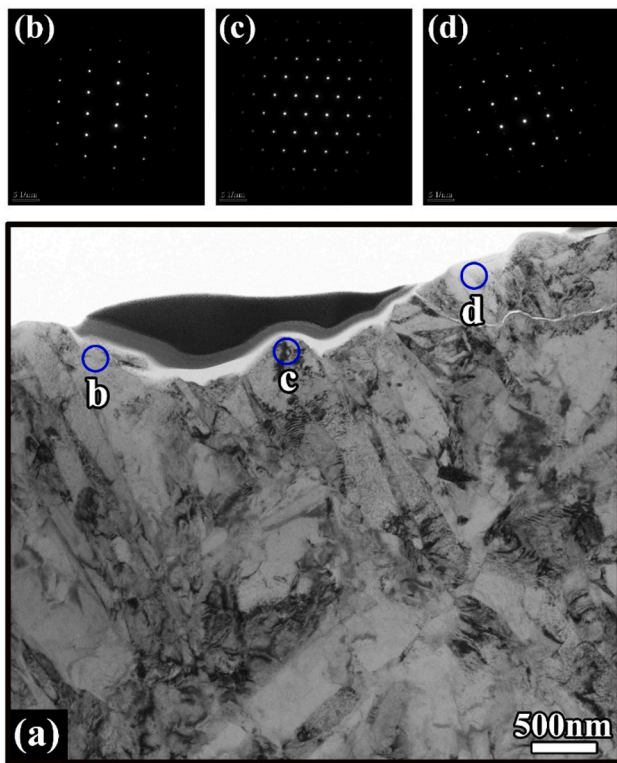
Fig. 8. Microstructure characterization at crack initiation site in HCF regime at $R = -1$, $\sigma_a = 300$ MPa, $N_f = 4.29 \times 10^5$: (a) BF image of sample P1; (b-d) SAD patterns at the locations underneath the fracture surface marked in (a).

defect is not a preferred spot for facet formation. In short, this investigation first reveals that two types of defects participate in the process of fatigue crack initiation for the SLMed Ti-6Al-4V. Type I defects (almost equiaxed) are the hot spots of crack initiation for the cases of $R = -1$ experienced HCF and VHCF, and those of $R = 0.5$ experienced HCF. Type II defects (large aspect ratio) act as crack origins only for the cases of $R = 0.5$ experienced VHCF, in which a facet domain of crack initiation zone prevails. This is a distinct crack initiation mechanism for the SLMed titanium alloy.

3.3. Microstructure refinement and nanograin formation at crack initiation region for VHCF under $R = -1$

For the purpose of detailed revelation of the microstructure characteristics in the crack initiation and early growth region under different stress ratios, five profile samples (P1, P2, P3, P4 and P5 shown in Figs. 4–6) were extracted from three fracture surfaces via FIB. Sample P1 was cut from the failed specimen ($\sigma_a = 300$ MPa, $N_f = 4.29 \times 10^5$) as shown in Fig. 4b, which failed due to surface defect in HCF regime at $R = -1$ without RA feature in crack initiation region. Samples P2 and P3 were cut from the failed specimen ($\sigma_a = 250$ MPa, $N_f = 1.85 \times 10^8$) as shown in Fig. 5b, which failed due to internal defect in VHCF regime at $R = -1$ with clear RA morphology in crack initiation region. Samples P4 and P5 were cut from the failed specimen ($\sigma_a = 90$ MPa, $N_f = 1.26 \times 10^8$) as shown in Fig. 6f, which failed due to internal defect in VHCF regime at $R = 0.5$ with the facet domain surrounding the defect.

Fig. 8 illustrates a TEM image with SAD examinations of sample P1 that was extracted from the specimen failed in HCF regime at $R = -1$, and the location of the TEM sample is just outside the surface defect as shown in Fig. 4b. The bright-field (BF) image of sample P1 shown in Fig. 8a presents the profile microstructure morphology underneath the selected location. It is seen that the feature is the original lamellar microstructure. The SAD patterns for the circular domains just

underneath the fracture surface (Fig. 8a) are shown in Fig. 8b-d. All the SAD patterns are regular isolated spots, indicating a single grain for every detected area. Therefore, it can be inferred that no microstructural changes occurred in the crack initiation site for the specimens failed in HCF regime at $R = -1$.

Fig. 9 shows the TEM images of profile samples P2 and P3 extracted from the fracture surface of the specimen failed in VHCF regime at $R = -1$, and the related SEM images of the broken specimen are shown in Fig. 5a and b. Sample P2 was extracted close to the internal defect inside the RA region, and sample P3 was extracted outside the RA region so that the microstructure characteristics both inside and outside the RA region can be examined. The BF image of sample P2 shown in Fig. 9a presents the microstructure feature underneath the RA region. It is seen that the microstructure is refined and the original lamellar feature disappears in the region underneath the fracture surface and above the dotted line. The dark-field (DF) image of sample P2 is shown in Fig. 9c. A layer containing many scattered bright micro-regions each with tens of nanometers is displayed near the fracture surface, suggesting the formation of nanograins underneath the fracture surface in the RA region. The thickness of the nanograin layer is between 500 and 1500 nm. Further, Fig. 9e-h show the SAD detections at the locations just underneath the fracture surface. The SAD patterns of the four locations e, f, g and h shown in Fig. 9a are all discontinuous diffraction rings, indicating there are several grains in every diffraction area (200 nm in diameter), which confirms the existence of nanograins. The formation of nanograins in the RA region is likely caused by the cyclic compression of the crack surfaces during the fatigue process. Therefore, for the case of crack initiation from internal defect in VHCF regime at $R = -1$, all results of the BF image, DF image and SAD patterns reveal the microstructure refinement and nanograin formation underneath the fracture surface in the RA region.

The microstructure feature of sample P3 is different from that of sample P2. Fig. 9b presents the BF image of sample P3 in the location just underneath the fracture surface outside the RA region, in which the original lamellar microstructure is presented. This result is similar to that of sample P1. The DF image of sample P3 (Fig. 9d) shows a more distinct morphology of original coarse grains, indicating no grain refinement occurred underneath the fracture surface outside the RA region. The SAD patterns (Fig. 9i-l) underneath the fracture surface are isolated spots, indicating that there is only one grain within the diffraction area. Therefore, it is inferred that no microstructure refinement and nanograin formation occurred underneath the fracture surface outside the RA region in VHCF regime at $R = -1$.

Fig. 10 shows the TEM images of samples P4 and P5 extracted from the fracture surface of the specimen failed in VHCF regime at $R = 0.5$. The related SEM images of the failed specimen are shown in Fig. 6d–f. As indicated in the previous section, for the specimens failed in the VHCF regime at $R = 0.5$, a facet formed surrounding the defect in the crack initiation region. As shown in Fig. 6f, sample P4 was extracted from the facet area near the defect, and sample P5 was extracted just outside the facet domain. Fig. 10a and b show the BF images of samples P4 and P5, respectively. Both BF images of the two samples display the original lamellar microstructure. The SAD patterns of sample P4 (Fig. 10e–h) and sample P5 (Fig. 10i–l) underneath the fracture surface are regular isolated diffraction spots, suggesting a single grain for every detected area. Therefore, it can be inferred that the process of microstructure refinement and nanograin formation does not occur in the crack initiation region for the specimen experienced VHCF at $R = 0.5$.

The results that nanograins formed in the crack initiation region under negative stress ratio ($R = -1$) while disappeared under positive stress ratio ($R = 0.5$) can be explained by the mechanism of "numerous cyclic pressing" (NCP) model [16,30]. For the case of negative stress ratio, the microstructure underneath the fracture surface inside the RA region is refined and there exists a nanograin layer with several hundred nanometers in thickness. The formation of nanograins can be ascribed to the severely contacting actions between the crack surfaces under
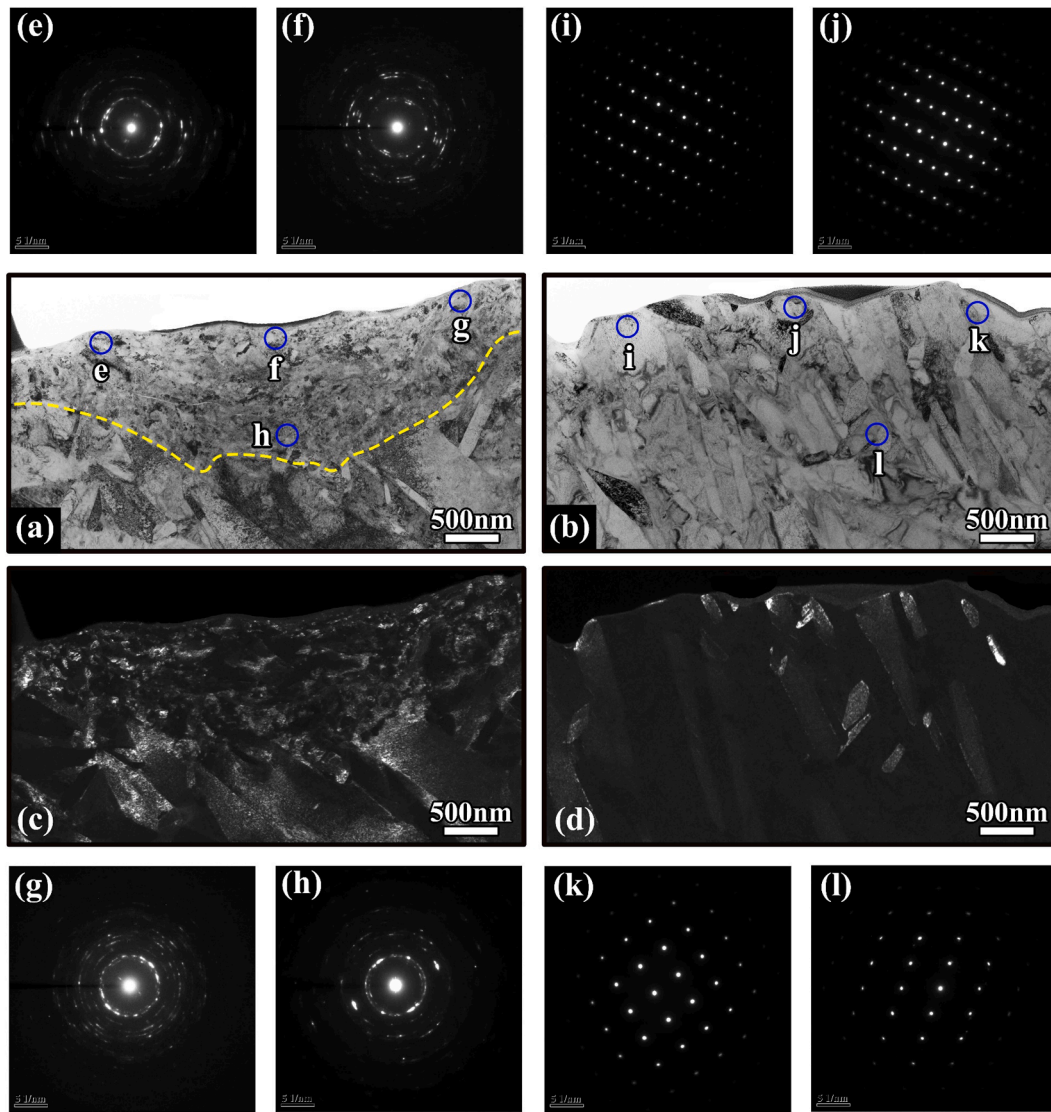
Fig. 9. Microstructure observations of samples P2 and P3 cut from fracture surface of the specimen failed in VHCF regime at $R = -1$, $\sigma_a = 250$ MPa, $N_f = 1.85 \times 10^8$. (a) BF image of sample P2, (b) BF image of sample P3, (c) DF image of sample P2, (d) DF image of sample P3, and (e-l) SAD patterns at the locations underneath the fracture surface marked in (a) and (b).

negative stress ratio cases with sufficient loading cycles. While for the cases of negative stress ratio in HCF regime and positive stress ratio in VHCF regime, no nanograins were found underneath the crack initiation region. This is another distinct crack initiation mechanism for the SLMed titanium alloy. This result together with our newly observations [40] is the first revelation of microstructure refinement and nanograin formation in the crack initiation region of the SLMed materials subjected to VHCF at $R = -1$.

3.4. Fatigue strength prediction model

In order to address the effect of stress ratio R on the VHCF responses of the SLMed Ti-6Al-4V, a model [41,42] was introduced to describe the fatigue life based on the obtained S-N data and the distribution of defect sizes. For this, the P-S-N curves at different stress ratios were first established and the VHCF strength was estimated by the model. The modeling steps are as follows.

Considering that both mean stress and stress amplitude have effects on the VHCF performance, we adopted the equivalent stress amplitude $\sigma_{a,eq}$ to establish the P-S-N model. According to Ref. [43], $\sigma_{a,eq}$ for different stress ratios is computed by "Smith-Watson-Topper" (SWT)

model:

$$\sigma_{a,eq} = \sigma_{max} \sqrt{\frac{1-R}{2}} \tag{2}$$

where σ_{max} is the maximum stress.

The P-S-N curves taking into account the defect size distribution were established according to the following equation [44]:

$$F_Y(y;x) = F_{Y,HCF}(y;x) F_{X_t}\left(\frac{x - \mu_{X_t}}{\sigma_{X_t}}\right) + F_{Y,VHCF}(y;x)\left[1 - F_{X_t}\left(\frac{x - \mu_{X_t}}{\sigma_{X_t}}\right)\right] \tag{3}$$

where

$$F_{Y,HCF}(y;x) = \int_0^\infty \Phi\left(\frac{y - \mu_{Y,HCF}\left(x, \sqrt{area_d}\right)}{\sigma_{Y,HCF}}\right) \cdot$$

$$f_{LEV}\left(\frac{\sqrt{area_d} - \mu_{\sqrt{area_d}}}{\sigma_{\sqrt{area_d}}}\right) d\sqrt{area_d} \text{ is the cumulative distribution function}$$

(cdf) of the finite fatigue life y in HCF regime, and $F_{Y,VHCF}(y;x) = \int_0^\infty$
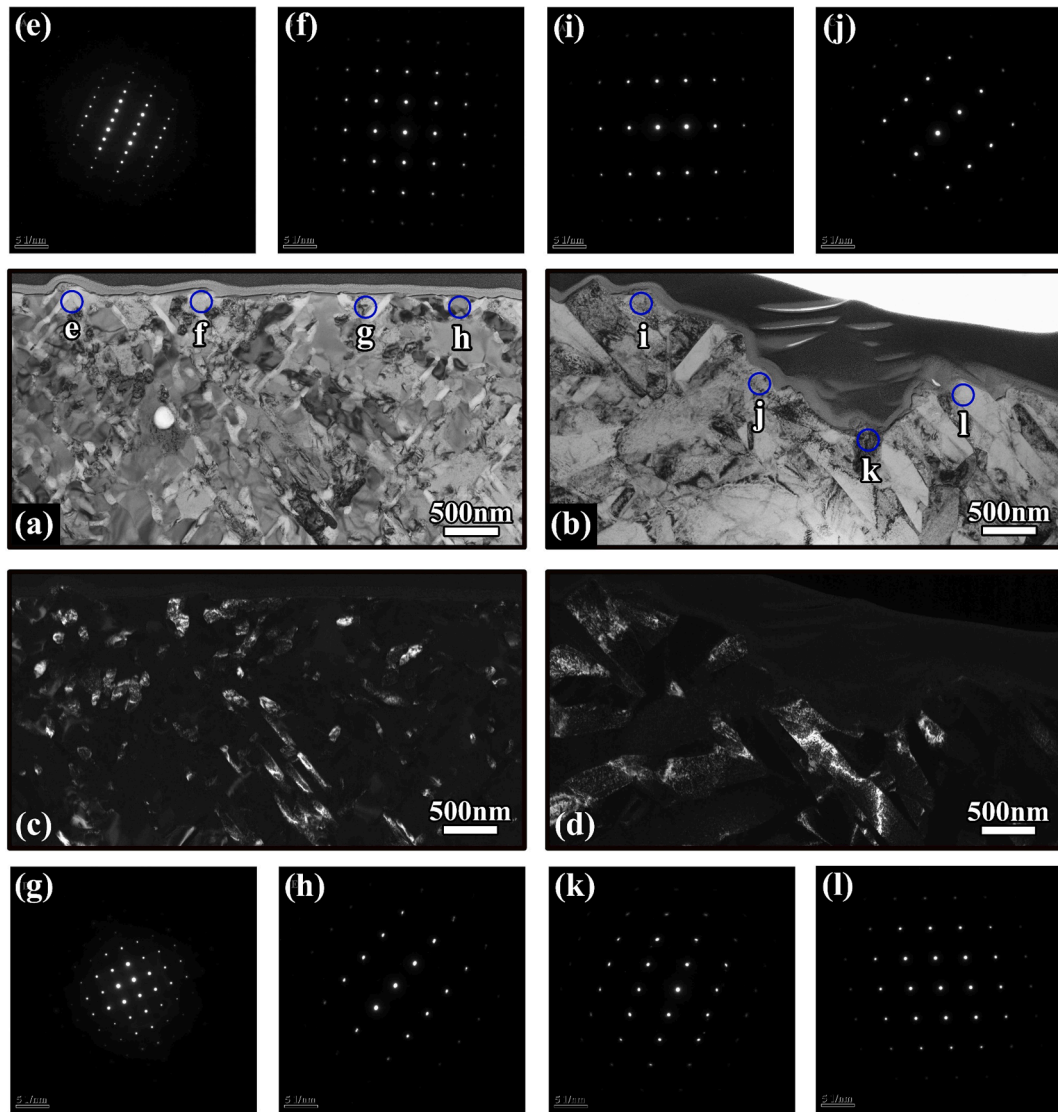
Fig. 10. Microstructure observations of TEM samples P4 and P5 cut from fracture surface of the specimen failed in VHCF regime at $R = 0.5$, $\sigma_a = 90$ MPa, $N_f = 1.26 \times 10^8$. (a) BF image of sample P4, (b) BF image of sample P5, (c) DF image of sample P4, (d) DF image of sample P5, and (e-l) SAD patterns at the locations underneath the fracture surface denoted in (a) and (b).
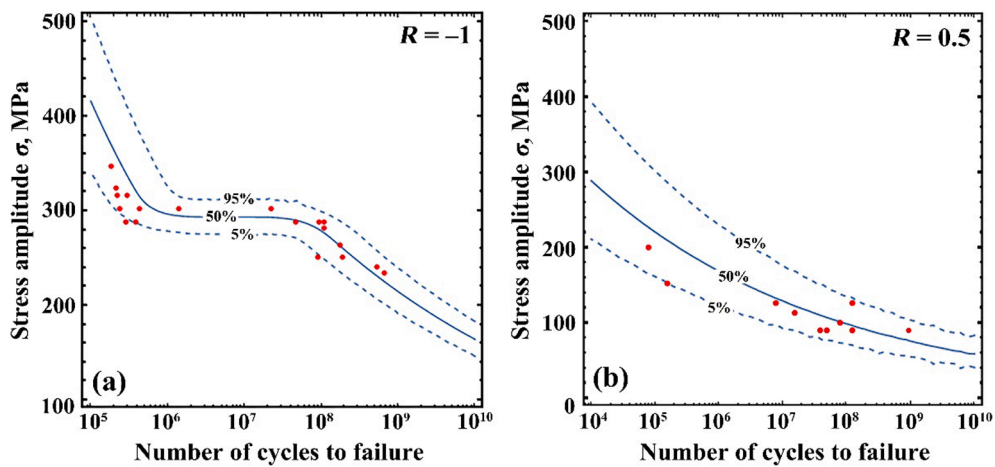

Fig. 11. Predicted P-S-N curves compared with experimental S-N data for the SLMed Ti-6Al-4V under two stress ratios: (a) $R = -1$, and (b) $R = 0.5$.
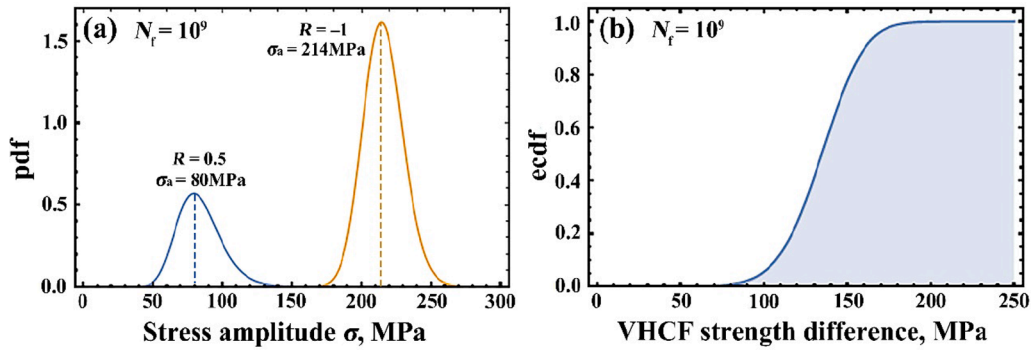
Fig. 12. (a) Pdfs for VHCF strength ($N_f = 10^9$ cycles) of the SLMed Ti-6Al-4V specimens and (b) ecdf for the difference between the VHCF strength.

$\Phi\left(\dfrac{y - \mu_{Y,\text{VHCF}}\left(x, \sqrt{area_d}\right)}{\sigma_{Y,\text{VHCF}}}\right) \cdot f_{\text{LEV}}\left(\dfrac{\sqrt{area_d} - \mu_{\sqrt{area_d}}}{\sigma_{\sqrt{area_d}}}\right) d\sqrt{area_d}$ is the cdf of the finite fatigue life y in VHCF regime. The fatigue life y is the logarithm of the number of cycles to failure ($y = \log_{10} N_f$) and x is the logarithm of the equivalent stress amplitude $\sigma_{a,eq}$. X_t is the transition stress of each specimen, which follows the normal distribution with mean value μ_{X_t} and standard deviation σ_{X_t}. $\Phi\left(\dfrac{y - \mu_{Y,\text{HCF}}\left(x, \sqrt{area_d}\right)}{\sigma_{Y,\text{HCF}}}\right)$ is the cdf of the normally distributed conditional finite fatigue life y, $\sqrt{area_d}$ is the initial defect size, $\mu_Y\left(x, \sqrt{area_d}\right) = c_Y + m_Y x + n_Y \log_{10} \sqrt{area_d}$, and σ_Y is the standard deviation. $f_{\text{LEV}}\left(\dfrac{\sqrt{area_d} - \mu_{\sqrt{area_d}}}{\sigma_{\sqrt{area_d}}}\right)$ is the probability density function (pdf) of the initial defect size $\sqrt{area_d}$, which follows the largest extreme value (LEV) distribution [44] with parameters $\mu_{\sqrt{area_d}}$ and $\sigma_{\sqrt{area_d}}$, as shown below

$$f_{\text{LEV}}\left(\frac{\sqrt{area_d} - \mu_{\sqrt{area_d}}}{\sigma_{\sqrt{area_d}}}\right) = \frac{1}{\sigma_{\sqrt{area_d}}} e^{\frac{\sqrt{area_d} - \mu_{\sqrt{area_d}}}{\sigma_{\sqrt{area_d}}}} \cdot e^{-e^{\frac{\sqrt{area_d} - \mu_{\sqrt{area_d}}}{\sigma_{\sqrt{area_d}}}}} \tag{4}$$

The coefficients of the mean fatigue life μ_Y and the standard deviation σ_Y in HCF and VHCF regimes have been estimated through a multiple linear regression. The coefficients ($\mu_{\sqrt{area_d}}$, $\sigma_{\sqrt{area_d}}$) of the LEV distribution were estimated through the application of the maximum likelihood principle by considering the defect size data. For the case of $R = -1$, two LEV distributions for defect size $\sqrt{area_d}$ in HCF and VHCF regimes were considered. While for the case of $R = 0.5$, only one LEV distribution for all defect size $\sqrt{area_d}$ was considered, regardless of fatigue life regime. Finally, the mean value μ_{X_t} and the standard deviation σ_{X_t} of the transition stress were estimated through the application of the maximum likelihood principle by considering Eq. (3) and all failed as well as runout specimens.

Fig. 11 presents the estimated P-S-N curves obtained by the model and the experimental S-N data for the SLMed Ti-6Al-4V under two stress ratios. It is seen that the 0.05-th, the 0.50-th and the 0.95-th quantiles (95% confidence interval) of the P-S-N curves show the good qualitative agreement with the experimental S-N data, which indicates that the fatigue life model can well describe the relationship among the fatigue strength, fatigue life, defect size and stress ratio for the SLMed Ti-6Al-4V subjected to the fatigue loading up to VHCF regime.

Then, for a proper and reliable assessment of the effect of stress ratio, the pdfs and the cdfs of the fatigue strengths at $N_f = 10^9$ cycles were estimated and compared with the experimental S-N data. The pdfs were calculated by deriving Eq. (3) with respect to y and then by setting $y = 9$ ($N_f = 10^9$). Fig. 12a shows the estimated pdfs for the fatigue strength (stress amplitude) at $N_f = 10^9$ cycles. The estimated VHCF strength fits well the experimental S-N data. It is seen that the mean stress amplitude at $N_f = 10^9$ cycles decreased from 214 MPa at $R = -1$ to 80 MPa at $R = 0.5$, indicating that the stress ratio significantly influences the VHCF strength. In addition, the cdfs for the stress amplitude at $N_f = 10^9$ cycles

were estimated by Monte Carlo method with 100,000 values of x from Eq. (3). In order to identify whether the difference between the fatigue strength at 10^9 cycles is statistically significant, the empirical cumulative distribution function (ecdf) [25] of the difference for the stress amplitude under two stress ratios was calculated based on the cdfs. Fig. 12b shows the variation of obtained ecdf with stress amplitude, indicating the variation of the difference in stress amplitude between the two stress ratios at $N_f = 10^9$ cycles. Obviously, the 5% quantile of the ecdf for the difference between the VHCF strength is much larger than zero. This also indicates that with the confidence level larger than 95%, the stress amplitude at $N_f = 10^9$ cycles under $R = -1$ is much larger than that under $R = 0.5$, which confirms that the difference between fatigue strength at 10^9 cycles under the two stress ratios based on the P-S-N model is significant. Therefore, the stress ratio considerably affects the VHCF response of the investigated SLMed Ti-6Al-4V. The introduced model taking into account the S-N data and the defect size distribution can well describe the fatigue strength at $N_f = 10^9$ cycles.

4. Conclusions

The fatigue behavior up to VHCF regime under two stress ratios of $R = -1$ and 0.5 for an SLMed Ti-6Al-4V was investigated and the crack initiation mechanisms at HCF and VHCF regimes were explicitly addressed. The main findings are as follows:

(1) Fatigue cracks initiated from lack-of-fusion defects in the SLMed Ti-6Al-4V. Surface defects caused crack initiation in HCF regime, and internal defects caused crack initiation in VHCF regime for both $R = -1$ and 0.5, with an RA feature surrounding the crack origin for $R = -1$, and without RA in the initiation site for $R = 0.5$.

(2) Two types of lack-of-fusion defects induced crack initiation. Type I defects (almost equiaxed) were the initiation sites for all cases at $R = -1$ and those of HCF at $R = 0.5$. Type II defects (large aspect ratio) with smaller equivalent size became the hot spots of crack initiation for the cases of VHCF at $R = 0.5$, and a facet domain formed surrounding the crack origin. This is ascribed to the high maximum stress in the cases of $R = 0.5$.

(3) The RA region is a nanograin layer only in the crack initiation region for the cases of VHCF under $R = -1$, which can be well explained by the NCP model. The compressive stress at the localized field of initiated crack surfaces caused crack closure, which promoted the grain refinement.

(4) A P-S-N model was introduced to describe the fatigue strength and fatigue life. The obtained P-S-N curves at different failure probabilities (5%, 50%, 95%) can well describe the S-N data under $R = -1$ and 0.5, and the fatigue strength at $N_f = 10^9$ cycles is well estimated.

Declaration of Competing Interest

The authors declare that they have no known competing financial interests or personal relationships that could have appeared to influence the work reported in this paper.

Acknowledgments

References

[1] Yadroitsev I, Krakhmalev P, Yadroitsava I, Johansson S, Smurov I. Energy input effect on morphology and microstructure of selective laser melting single track from metallic powder. J Mater Process Technol 2013;213:606–13.

[2] Rodriguez OL, Allison PG, Whittington WR, Francis DK, Rivera OG, Chou K, et al. Dynamic tensile behavior of electron beam additive manufactured Ti6Al4V. Mater Sci Eng A 2015;641:323–7.

[3] Kumar P, Prakash O, Ramamurty U. Micro-and meso-structures and their influence on mechanical properties of selectively laser melted Ti-6Al-4V. Acta Mater 2018;154:246–60.

[4] Marten T, Emmelmann C, Brandt M, Pateras A. Measurement of actual powder layer height and packing density in a single layer in selective laser melting. Addit Manuf 2019;28:176–83.

[5] Zhou X, Wang D, Liu X, Zhang D, Qu S, Ma J, et al. 3D-imaging of selective laser melting defects in a Co-Cr-Mo alloy by synchrotron radiation micro-CT. Acta Mater 2015;98:1–16.

[6] Hojjatzadeh S, Parab N, Yan W, Guo Q, Xiong L, Zhao C, et al. Pore elimination mechanism during 3D printing of metals. Nat Commun 2019;10:3088.

[7] Siddique S, Imran M, Walther F. Very high cycle fatigue and fatigue crack propagation behavior of selective laser melted AlSi12 alloy. Int J Fatigue 2017;94:246–54.

[8] Azizi H, Zurob H, Bose B, Ghiaasiaan SR, Wang X, Coulson S, et al. Additive manufacturing of a novel Ti-Al-V-Fe alloy using selective laser melting. Addit Manuf 2018;21:529–35.

[9] Günther J, Krewerth D, Lippmann T, Leuders S, Tröster T, Weidner A, et al. Fatigue life of additively manufactured Ti-6Al-4V in the very high cycle fatigue regime. Int J Fatigue 2017;94:236–45.

[10] Yamashita Y, Murakami T, Mihara R, Okada M, Murakami Y. Defect analysis and fatigue design basis for Ni-based superalloy 718 manufactured by selective laser melting. Int J Fatigue 2018;117:485–95.

[11] Biswal R, Syed AK, Zhang X. Assessment of the effect of isolated porosity defects on the fatigue performance of additive manufactured titanium alloy. Addit Manuf 2018;23:433–42.

[12] Yadollahi A, Shamsaei N. Additive manufacturing of fatigue resistant materials: Challenges and opportunities. Int J Fatigue 2017;98:14–31.

[13] Yadollahi A, Mahmoudi M, Elwany A, Doude H, Bian L, Newman Jr JC. Fatigue-life prediction of additively manufactured material: Effects of heat treatment and build orientation. Fatigue Fract Eng Mater Struct 2020;43:831–44.

[14] Leuders S, Vollmer M, Brenne F, Tröster T, Niendorf T. Fatigue strength prediction for titanium alloy TiAl6V4 manufactured by selective laser melting. Metall Mater Trans A 2015;46(9):3816–23.

[15] Bathias C. There is no infinite fatigue life in metallic materials. Fatigue Fract Eng Mater Struct 1999;22:559–65.

[16] Hong Y, Sun C. The nature and the mechanism of crack initiation and early growth for very-high-cycle fatigue of metallic materials – An overview. Theor Appl Fract Mech 2017;92:331–50.

[17] Yoshinaka F, Nakamura T, Takeuchi A, Uesugi M, Uesugi K. Initiation and growth behaviour of small internal fatigue cracks in Ti-6Al-4V via synchrotron radiation microcomputed tomography. Fatigue Fract Eng Mater Struct 2019;42:2093–105.

[18] McEvily AJ, Nakamura T, Oguma H, Yamashita K, Matsunaga H, Endo M. On the mechanism of very high cycle fatigue in Ti-6Al-4V. Scripta Mater 2008;59:1207–9.

[19] Heinz S, Balle F, Wagner G, Eifler D. Analysis of fatigue properties and failure mechanisms of Ti6Al4V in the very high cycle fatigue regime using ultrasonic technology and 3D laser scanning vibrometry. Ultrasonics 2013;53:1433–40.

[20] Akerfeldt P, Pederson R, Antti M. A fractographic study exploring the relationship between the low cycle fatigue and metallurgical properties of laser metal wire deposited Ti-6Al-4V. Int J Fatigue 2016;87:245–56.

[21] Ren YM, Lin X, Guo PF, Yang HO, Tan H, Chen J, et al. Low cycle fatigue properties of Ti-6Al-4V alloy fabricated by high-power laser directed energy deposition: experimental and prediction. Int J Fatigue 2019;127:58–73.

[22] Pegues J, Roach M, Williamson R, Shamsaei N. Surface roughness effects on the fatigue strength of additively manufactured Ti-6Al-4V. Int J Fatigue 2018;116:543–52.

[23] Fatemi A, Molaei R, Simsiriwong J, Sanaei N, Pegues J, Torries B, et al. Fatigue behaviour of additive manufactured materials: an overview of some recent experimental studies on Ti-6Al-4V considering various processing and loading direction effects. Fatigue Fract Eng Mater Struct 2019;42:991–1009.

[24] Günther J, Krewerth D, Lippmann T, Leuders S, Tröster T, Weidner A. Fatigue life of additively manufactured Ti–6Al–4V in the very high cycle fatigue regime. Int J Fatigue 2017;94:236–45.

[25] Qian G, Li Y, Paolino D, Tridello A, Berto F, Hong Y. Very-high-cycle fatigue behavior of Ti-6Al-4V manufactured by selective laser melting: effect of build orientation. Int J Fatigue 2020;136:105628.

[26] Du L, Qian G, Zheng L, Hong Y. Influence of processing parameters of selective laser melting on high-cycle and very-high-cycle fatigue behaviour of Ti-6Al-4V. Fatigue Fract Eng Mater Struct 2021;44:240–56.

[27] Liu X, Sun C, Hong Y. Effects of stress ratio on high-cycle and very-high-cycle fatigue behavior of a Ti-6Al-4V alloy. Mater Sci Eng A 2015;622:228–35.

[28] Pan X, Hong Y. High-cycle and very-high-cycle fatigue behavior of a titanium alloy with equiaxed microstructure under different mean stresses. Fatigue Fract Eng Mater Struct 2019;42:1950–64.

[29] Pan X, Xu S, Qian G, Nikitin A, Shanyavskiy A, Palin-Luc T, et al. The mechanism of internal fatigue-crack initiation and early growth in a titanium alloy with lamellar and equiaxed microstructure. Mater Sci Eng A 2020;798:140110.

[30] Hong Y, Liu X, Lei Z, Sun C. The formation mechanism of characteristic region at crack initiation for very-high-cycle fatigue of high-strength steels. Int J Fatigue 2016;89:108–18.

[31] Su H, Liu X, Sun C, Hong Y. Nanograin layer formation at crack initiation region for very-high-cycle fatigue of a Ti-6Al-4V alloy. Fatigue Fract Eng Mater Struct 2017;40:979–93.

[32] Thijs L, Verhaeghe F, Craeghs T, Van Humbeeck J, Kruth J. A study of the microstructural evolution during selective laser melting of Ti–6Al–4V. Acta Mater 2010;58:3303–12.

[33] Xu W, Lui E, Pateras A, Qian M, Brandt M. In situ tailoring microstructure in additively manufactured Ti-6Al-4V for superior mechanical performance. Acta Mater 2017;125:390–400.

[34] Liang Z, Sun Z, Zhang W, Wu S, Chang H. The effect of heat treatment on microstructure evolution and tensile properties of selective laser melted Ti6Al4V alloy. J. Alloys Compd 2019;782:1041–8.

[35] Shayesteh N, Saghaian S, Amerinatanzi A, Ibrahim H, Li P, Toker G, et al. Anisotropic tensile and actuation properties of NiTi fabricated with selective laser melting. Mater Sci Eng A 2018;724:220–30.

[36] Beese AM, Carroll BE. Review of mechanical properties of Ti-6Al-4V made by laser-based additive manufacturing using powder feedstock. JOM 2016;68:724–34.

[37] Simonelli M, Tse YY, Tuck C. Effect of the build orientation on the mechanical properties and fracture modes of SLM Ti–6Al–4V. Mater Sci Eng A 2014;616:1–11.

[38] Zhang M, Sun C, Zhang X, Goh P, Wei J, Hardacre D, et al. Fatigue and fracture behaviour of laser powder bed fusion stainless steel 316L: Influence of processing parameters. Mater Sci Eng A 2017;703:251–61.

[39] Afkhami S, Dabiri M, Habib S, Björk T, Salminen A. Fatigue characteristics of steels manufactured by selective laser melting. Int J Fatigue 2019;122:72–83.

[40] Li Y, Qian G, Hong Y, Kumar P. Microstructure evolution of crack initiation region under very-high-cycle fatigue for Ti-6Al-4V manufactured by selective laser melting. 2021, submitted.

[41] Paolino D, Chiandussi G, Rossetto M. A unified statistical model for S-N fatigue curves: probabilistic definition. Fatigue Fract Eng Mater Struct 2012;36:187–201.

[42] Paolino D, Tridello A, Chiandussi G, Rossetto M. S-N curves in the very-high-cycle fatigue regime: statistical modeling based on the hydrogen embrittlement consideration. Fatigue Fract Eng Mater Struct 2016;39:1319–36.

[43] Smith K. A stress-strain function for the fatigue of metals. J Mater 1970;5:767–78.

[44] Murakami Y. Metal Fatigue: Effects of Small Defects and Nonmetallic Inclusions. London: Elsevier; 2002.